Finite Element Navier-Stokes Calculation of Three-Dimensional Turbulent Flow Near a Propeller

D. H. Pelletier*
Ecole Polytechnique, Montreal, Canada
and
J. A. Schetz†
Virginia Polytechnic Institute and State University, Blacksburg, Virginia

A numerical procedure based on the primitive variable Navier-Stokes equations is applied to the simulation of the three-dimensional flow near a propeller in a shear flow. The Navier-Stokes equations are solved by a penalty function finite element method. The propeller is modeled as an actuator disk, and the direct simulation of a given propeller is considered in detail. Turbulent transport is modeled by an integrated turbulent kinetic energy equation. This approach results in a robust numerical algorithm. Detailed comparison with wind tunnel measurements show good prediction of velocity and pressure. The high accuracy of the swirl prediction is a major improvement over previous analyses.

Nomenclature

A	= cross section of the flowfield and area of the propeller
a_2, c_2	= constants in the turbulence model
D	= domain of solution and propeller diameter
k	= turbulence kinetic energy
K_Q, K_T	= torque and thrust coefficients, respectively
N	= rotational speed of the propeller
n_j	= unit outward normal
P	= pressure
Q	= torque of the propeller
$r_{1/2}$	= half-width of shear layer
Re	= Reynolds number
s	= radial distribution of swirl force
S	= boundary of the domain D
t	= distribution of thrust
t_i	= surface traction vector
T	= thrust of the propeller
U_i	= velocity vector
U_{inf}	= upstream approach flow
ϵ	= turbulence viscous dissipation
λ	= penalty parameter
ρ	= density of the fluid

Introduction

DETAILED analysis of the three-dimensional flow produced by a propeller/body combination is of interest in a number of practical applications. Examples include the influence of the propeller on the body pressure distribution, the prediction of the near-wake profiles, cyclic loading to produce vibrations, and the influence of a downstream surface on a propeller and vice versa, to name a few. Until recently, only approximate treatments were available involving one or more of the following restrictive assumptions: the flow was assumed inviscid; the propeller was represented as an actuator disk with constant thrust; the flow was taken as laminar, and/or the effects of the propeller on the flowfield were assumed small enough to permit linearization of the equations of motion. References 1-3 are representative.

The numerical solution procedure reported in Refs. 4-6 had as its goal the development of a realistic treatment, holding simplifying assumptions and approximations to a minimum. The work was based on the full, axisymmetric, mean (in the turbulence sense), unsteady Navier-Stokes equations. In order to place some bounds on the scope of the effort at that time, however, some simplifications were necessary. The first was the assumption of an actuator disk model for the propeller, although arbitrary radial variations of thrust were allowed. Second, the flow was taken as axisymmetric. Third, turbulent transport processes were described by an integrated, turbulence-kinetic-energy (TKE) model, which was used to predict an eddy viscosity distribution. The unsteady equations of motions were cast in terms of a stream function, one vorticity component, and the peripheral velocity. Comparison of the predictions of this procedure with laboratory data for an axisymmetric flow showed good agreement for the axial velocity component. The swirl velocity component predictions were consistently too low.

From the point of view of direct applications to problems of practical interest, the biggest limitation to the analysis described above is its restriction to two-dimensional axisymmetric flows. Actual propeller-driven vehicles have either a three-dimensional body near the propeller and/or appendages that render the flow three-dimensional. For many cases, the assumption of an actuator disk representation of the propeller remains appropriate, while the restriction to axisymmetric flow does not. Furthermore, the jump to trying to treat the three-dimensional, cyclically unsteady problem with individual blades with their thin boundary layers and wakes is too great to be attempted in one step at this time.

The present work is part of a step-by-step approach to the development of a computational method for analysis of propeller flowfields with three-dimensional inflows and the effects of appendages in situations of increasing complexity and practical realism. The fully elliptic, three-dimensional, time-averaged, steady-state, primitive-variables Navier-Stokes equations are solved by a penalty finite element method because of its ease of handling complicated geometries and its simplicity for implementing a variety of boundary conditions. Turbulence modeling is done through a generalization of the integrated TKE model of Refs. 4-6.

Presented as Paper 85-0365 at the AIAA 23rd Aerospace Sciences Meeting, Reno, NV, Jan. 14-17, 1985; received Feb. 26, 1985; revision received Dec. 16, 1985.

*Research Fellow; also Adjunct Professor, Aerospace and Ocean Engineering, Virginia Polytechnic Institute and State University. Member AIAA.

†Professor and Department Head. Fellow AIAA.

Modeling of the Problem

Equations of Motion

The mean flow equations in Cartesian coordinates are given by

$$U_{i,i}=0 \tag{1}$$

$$\rho U_j U_{i,j}=-P_{,i}+\rho f_i+[\mu_T(U_{i,j}+U_{j,i})]_{,j} \tag{2}$$

where μ_T is the turbulent eddy viscosity and f_i are body forces representing the effects of the propeller disk.

Turbulence Model

Following Refs. 4-6, a simple turbulence model is used, since little experimental data are available for this type of problem on which to base more elaborate models. An integrated form of the TKE equation is used (details of the algebraic manipulations are contained in Ref. 7):

$$\frac{\mathrm{d}}{\mathrm{d}x}\left(\iint_A \rho U k\,\mathrm{d}A\right)=\iint_A \nu_T[(U_{,y})^2+(U_{,z})^2 + (V_{,z}+W_{,y})^2]\,\mathrm{d}A+\iint_A \epsilon\,\mathrm{d}A \tag{3}$$

In order to close the model, the TKE must be related to the eddy viscosity $\mu_T=\rho\nu_T$. This is done through the use of the Prandtl-Kolmogorov relationship[8]

$$\nu_T=c_2 k^{1/2} L \tag{4}$$

Assuming that viscous dissipation is important only in the inertial subrange, dimensional consistency dictates that the viscous dissipation be modeled as[8]

$$\epsilon=a_2 k^{3/2}/L \tag{5}$$

where L is a characteristic length scale of the shear layer and a_2 and c_2 are constant. Physically, all integrands in Eq. (3) are sufficiently well behaved to ensure boundedness of the integrals. The assumption that the eddy viscosity is constant over the cross section of the flow is a well-documented behavior for free shear flows. In fact, the eddy viscosity is constant over most of the shear layer and decays to zero only as the radial distance r from the x axis goes to infinity. In order to preserve this behavior and ensure boundedness of the integrals in the modeled integrated equation, we introduce a distribution function γ, representing the distribution of μ_T across the layer. It is closely related to the actual intermittency of the turbulent flow. The following form, obtained from a nonlinear least-squares fit to intermittency data for a turbulent boundary layer over a flat plate and turbulent plane and round jets, was found satisfactory:

$$\gamma=\gamma_y\gamma_z$$

where

$$\gamma_y=0.5[1-\mathrm{erf}(1.98Y/Y_{1/2}-3.42)]$$

$$\gamma_z=0.5[1-\mathrm{erf}(1.98Z/Z_{1/2}-3.42)]$$

and $Y_{1/2}$ and $Z_{1/2}$ are the half-widths of the shear layer along the y and z axes, respectively. The half-widths are defined by the points on the Y and Z axes, where

$$(U-U_{\inf})/(U-U_{\inf})_{\max}=0.5$$

In this expression, $U_{\inf}$ is the freestream approach flow velocity that can be nonuniform.

It should be noted that the particular form of the distribution function used is not critical. Choosing different algebraic forms will simply result in slightly different values of the constant a_2 and c_2.

Upon substitution of Eqs. (4) and (5) into Eq. (3), the modeled integrated TKE equation takes the form

$$\frac{\mathrm{d}\nu_T}{\mathrm{d}x}=\frac{0.5}{Y_1}\left(Y_2-\nu_T\frac{\mathrm{d}}{\mathrm{d}x}Y_1-\nu_T^2 Y_3\right) \tag{6}$$

where

$$Y_1=\iint_A \frac{U\gamma^2}{(c_2^2 L)}\,\mathrm{d}A$$

$$Y_2=\iint_A \gamma[(U_{,y})^2+(U_{,z})^2+(V_{,z}+W_{,y})^2]\,\mathrm{d}A$$

$$Y_3=\iint_A \frac{\gamma a_2}{(c_2^3 L)}\,\mathrm{d}A$$

It now remains to specify the length scale L. Following Ref. 9, we adopt

$$L=[(Y_{1/2}^a Z_{1/2}^a)/(Y_{1/2}^a+Z_{1/2}^a)]^{1/a}$$

with $a=1.89$. This ensures correct dependence for the limiting cases of planar and axisymmetric flows. Equation (6) is an initial value problem for the kinematic eddy viscosity ν_T. The only data required is an initial condition for ν_T at the upstream inflow boundary, a value that can be easily estimated for most flows. One significant advantage of the present model is the absence of the diffusion of TKE, a most difficult term to model.

The present model was calibrated on the simple, well-documented turbulent flow problem of the far field of a round jet issuing into still surroundings. This flow has an analytical solution[10] for the velocity field, and the value of the eddy viscosity is known and constant. The integrals are evaluated exactly and, with the assumption of turbulence equilibrium, the constants are determined to be[7]

$$a_2=0.519 \qquad c_2=0.154$$

Modeling of the Propeller

The propeller is modeled by a disk of radius equal to the propeller radius and of thickenss Δx, roughly equal to the physical thickness of the propeller. The thrust and torque are allowed to vary radially but are constant in the tangential direction. Little is known about the detailed radial thrust and torque distributions of a given propeller. Generally, one only knows the global values of total thrust and torque. For simplicity we use a trapezoidal distribution given by

$$\begin{aligned}
&t(r)=0 && r \text{ in } [0,r_1]\\
&t(r)=t_m(r-r_1)/(r_2-r_1) && r \text{ in } [r_1,r_2]\\
&t(r)=t_m && r \text{ in } [r_2,r_3]\\
&t(r)=t_m(R-r)/(R-r_3) && r \text{ in } [r_3,R]\\
&t(r)=0 && r>R
\end{aligned} \tag{7}$$

where t_m is the maximum value of the thrust and R is the radius of the propeller. Values of r_1, r_2, and r_3 were set to $0.25R$, $0.7R$, and $0.85R$, respectively. These values result in distributions similar to those of Refs. 4-6. The same form is adopted for the distribution of the force s producing the swirl. Its maximum value is denoted by s_m. The upstream face of the propeller disk is located at $x=-\Delta x$, while the

back face of the propeller is located at $x=0.0$. These distributions are integrated to yield the global thrust and torque of the propeller:

$$T=0.3075*2\pi*R^2*t_m \tag{8}$$

$$Q=0.2218*2\pi*R^3*s_m \tag{9}$$

Given values of the global thrust and torque, the values of t_m and s_m are determined from Eqs. (8) and (9).

The corresponding body forces used in the finite element code are obtained by dividing the thrusting and swirling forces by the thickness of the propeller disk. It is assumed that the axial distribution of body forces is uniform throughout the thickness of the disk. The disk thickness is set to 0.041 propeller diameter, a dimension that corresponds roughly to the axial thickness of the propeller used in the experiments.

Solution Algorithm

Penalty Function Formulation

Details of the weak Galerkin formulation are readily available for penalty function formulations.[11] Thus, only an outline of the technique is presented here.

Substitution of an approximate solution (U^*,P^*) into Eqs. (1) and (2) yields a set of residual equations of the form

$$\text{Momentum:} \quad f_1(U^*,P^*)=R_1$$

$$\text{Continuity:} \quad f_2(U^*)=R_2$$

where R_i are the residuals, a measure of the quality of the approximate solution used. The Galerkin method reduces this error to zero, in a weighted sense, by making the residuals orthogonal to some set of functions. The weighting functions δU_i must satisfy the continuity equation. The continuity equation constraint is enforced by use of a penalty method. The resulting weak formulation is given by[7,11]

$$\int_D \{\delta U_i \rho U_j U_{i,j} + \delta U_{i,j}\mu_T(U_{i,j}+U_{j,i}) + \delta U_i \rho f_i\}\,dD$$

$$+\lambda\int_D U_{i,i}\delta U_{i,i}\,dD = \int_S \delta U_i t_i\,dS \tag{10}$$

Here λ is a positive number whose value affects the accuracy of the solution, while δU_i may be interpreted as a virtual velocity and Eq. (10) is similar to the principle of virtual work of solid mechanics.

The divergence theorem was applied to the pressure and viscous terms to reduce the differentiability requirement on the velocity by transferring some of the derivative from U_i to δU_i and to introduce the natural boundary conditions involving the surface tractions or forces t_i:

$$t_i=[-P+\mu_T(U_{i,j}+U_{j,i})]n_j$$

The pressure does not appear explicitly in Eq. (10); it appears only implicitly through the surface integrals on the right-hand side of Eq. (10). The only unknowns are the velocity components. This results in significant computational savings. Once the velocity field is obtained by solving Eq. (10), the pressure may be computed in a postprocessing step from the following relationship:[7,11]

$$P=-\lambda U_{i,i} \tag{11}$$

Convergence of the solution of the penalty formulation to the true solution, as $\lambda\to\infty$, can be proved.[12] A value of λ of 10^6 to 10^8 usually proves effective.

For reasons of computational economy, we use the trilinear velocity, constant pressure element.[11] This element, under certain circumstances, may suffer from spurious pressure solutions. Our experience with this element indicates that it is a fairly reliable element for the problems treated here. No spurious pressure solutions were observed.

General Solution Procedure

The formulation results in a system of nonlinear algebraic equations of the form

$$K[U,\nu_T(U)]U=F$$

where K is the global system matrix, U the global vector of unknowns, and F the global vector of body forces and boundary conditions.

This system of equations may be solved by a combination of methods: successive substitution, Newton-Raphson, and quasi-Newton methods.[13] The Newton method converges quadratically while the quasi-Newton procedure converges superlinearly. However, the cost of a quasi-Newton iteration is about 10-15% of that for a Newton iteration. In practice, the use of quasi-Newton iteration results in substantial computational savings for a given tolerance of the global iteration scheme.

The following iteration strategy was found suitable throughout this study: starting from a first guess for the velocity field, the quasi-Newton method is used to iterate until convergence. The eddy viscosity distribution is updated at each iteration by solving Eq. (6) using the current velocity distribution to evaluate the coefficients of the ordinary differential equation. The linearized system of equations is very large and is solved by direct Gaussian decomposition in a compacted, skyline, out-of-core solver.[14]

Results and Discussion

The turbulence model was programmed and interfaced to the general-purpose finite element fluid dynamics program FIDAP.[15] The resulting code can simulate planar, axisymmetric, and three-dimensional turbulent free shear flows.

Nondimensionalization

All calculations were performed with a nondimensional form of the equations of motion for the conditions of Ref. 16. Reference values are selected for the velocity U_0^*, length L_0^*, and pressure P_0^* to obtain the following dimensionless variables (the star denotes a dimensional variable):

$$x_i=x_i^*/L_0^*, \quad U_i=U_i^*/U_0^*$$

$$P=(P^*-P_0^*)/(\rho^*U_0^{*2})$$

$$\mu_T=\mu_T^*/(\rho^*U_0^*L_0^*)=1/Re_{\mu_T}$$

$$f=f^*/(U_0^{*2}/L_0^*), \quad \rho=\rho^*/\rho_0^*=1$$

Initial Value for the Eddy Viscosity

The absence of solid walls or aftbody upstream of the propeller in the present idealized flow problem results in an undisturbed, inviscid, uniform or shear approach flow, making difficult the determination of the initial condition for the turbulence model. The flow through and past a propeller has many of the characteristics of a turbulent jet.[17] Hence, an indication of the magnitude of μ_T may be obtained from the standard jet formula for the eddy viscosity:[17]

$$\nu_T=0.025 r_{1/2}\Delta U$$

where $r_{1/2}$ is the half-width of the layer and can be taken as $r_{1/2}=R$, the radius of the propeller, and ΔU is the character-

istic velocity excess determined from a simplified, inviscid one-dimensional analysis of the propeller:[18]

$$\Delta U^* = [2T^*/(\rho^* A) + V_0^{*2}]^{1/2} - U_0^*$$

The following data apply to the uniform flow of Ref. 16:

$$R^* = 0.246 \text{ m}, \quad U_0^* = 8.52 \text{ m/s}, \quad T^* = 2.914 \text{ N}$$

$$A^* = 0.19 \text{ m}^2, \quad \rho^* = 1.177 \text{ kg/m}^3, \quad \Delta U^* = 1.41 \text{ m/s}$$

A rough estimate of the eddy viscosity downstream of the propeller is, in dimensionless form,

$$\mu_T = \nu_T^*/(DU_0) = 0.002$$

There remains to select an initial value for the eddy viscosity. Assuming that the Prandtl-Kolmogorov relationship holds, we have

$$\nu_{T_{\text{init}}}^* = 0.2 k_0^{1/2} R$$

where $c = 0.2$ (the value for jets) and k_0 is the turbulence intensity upstream of the propeller. The corresponding dimensionless form is

$$\nu_{T_{\text{init}}} = \nu_{T_{\text{init}}}^*/(U_0 D) = 0.1 k_0^{1/2}/U_0$$

From the experiments of Ref. 16, we have

$$k_0^{*1/2}/u_0^* = 0.01$$

and an estimate of the initial eddy viscosity is finally

$$\nu_{T_{\text{init}}} = 0.001$$

To assess the validity of this analysis and to investigate the effect of the choice of the initial value of the eddy viscosity distribution, simulations were performed for the uniform flow of Ref. 16. The calculations were done for an axisymmetric flow without swirl.

Figure 1 shows that low values of μ_T in the range 10^{-5}-10^{-3} produce similar results, with a peak eddy viscosity of 0.0025, a value in good agreement with our rough estimate of 0.002. Higher initial values produce distributions that are probably too high. The bottom four curves result in clustered distributions well within the margin of uncertainty for this problem. An initial value of $5*10^{-4}$ was judged adequate and used for all subsequent simulations.

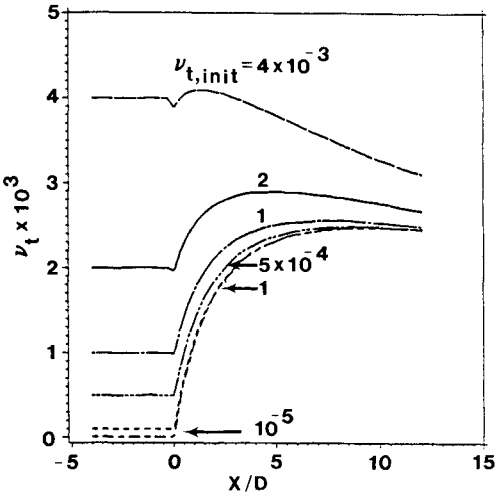

Fig. 1 Effect of initial value of eddy viscosity.

Table 1 Global matrix characteristics

	Penalty	Mixed
NEQ[a]	10 557	14 145
NEM[b]	10 997 103	19 434 905
MINB[c]	521	687
MAXB[d]	886	1 186

[a]Number of equations. [b]Number of matrix coefficients stored. [c]Average bandwidth of the matrix. [d]Maximum bandwidth.

Computational Savings Arising from the Use of the Penalty Method

To illustrate the computational savings afforded by the use of the penalty method, we present the characteristics of the global stiffness matrix of the three-dimensional propeller simulations for the penalty and velocity pressure (mixed) formulations (see Table 1). The mesh has a total of 3768 nodes and 3588 eight-noded brick elements (see Fig. 2).

In Table 1, the mixed formulation has 34% more unknowns, has a bandwidth 32% greater, and stores 77% more matrix coefficients. The Gaussian L-U factorization time is 2- and 5-h CPU for the penalty and mixed methods, respectively (on IBM-3081, using FORTRAN-H extended with optimization level 1). Clearly, the penalty method offers substantial savings.

Uniform Flow Past a Propeller

The characteristics of the flow are:

$$U_0^* = 8.52 \text{ m/s}, \quad \rho_0^* = 1.177 \text{ kg/m}^3, \quad D^* = 0.492 \text{ m}$$

$$N = 1150 \text{ rpm}, \quad K_T = T/(\rho_0^* N^2 D^{*4}) = 0.150$$

$$K_Q = Q/(\rho_0^* N^2 D^{*5}) = 0.0279$$

The grid is a cylinder with 24 nodes in the axial direction, 14 in the radial direction, and 12 in the peripheral direction. The inflow boundary is located 2 diameters upstream of the propeller (see Fig. 2). The outflow plane stands at 3 diameters downstream of the disk, while the freestream boundary is a cylindrical shell of radius 1.2 diameters. At the inflow, U is set to unit value and V and W are set to zero. On the freestream boundary, U is set to 1 and the y and z tractions are set to zero. The three components of the traction vector are set to zero at the outflow boundary.

The mean flow quantities are not all predicted or measured with the same accuracy. For the present finite element scheme, the three velocity components are the most accurately predicted, while the pressure prediction is less accurate. For the experiments of Kotb,[16] the order of decreasing accuracy in the measurements of the mean flow properties is: axial velocity, pressure, swirl, and lastly radial velocity. It should also be noted that while the finite element simulations can accurately represent a free-running propeller, the experiments must use a shaft to support and drive the propeller. A body must be placed close to and downstream of the propeller to house the drive train.[16] The housing begins at 0.23 propeller diameter downstream of the disk. The presence of the housing will probably affect the ex-

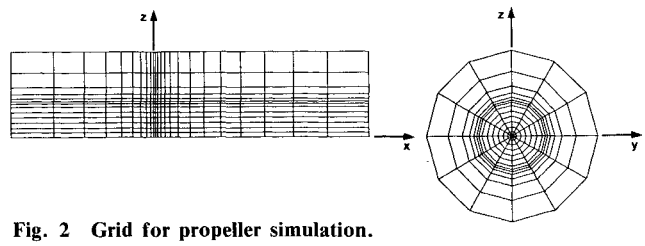

Fig. 2 Grid for propeller simulation.

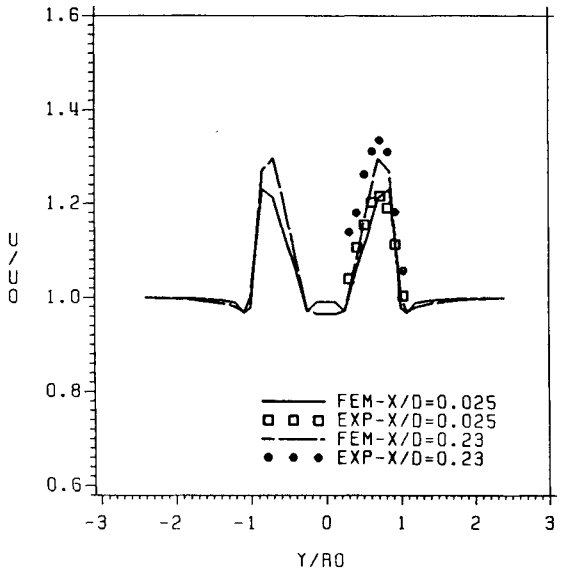

Fig. 3 Uniform flow: axial velocity profile.

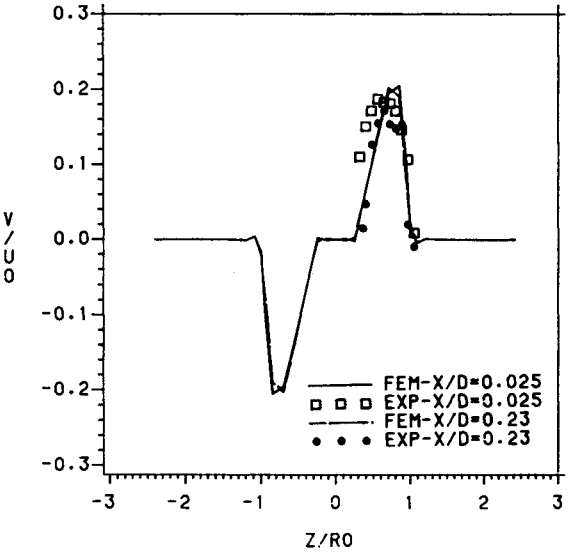

Fig. 4 Uniform flow: swirl profile.

perimental results from the station located at $x/D=0.23$ since this station sits right on the body.

Figure 3 compares the experimental and predicted axial velocity profiles along the y axis. The agreement is excellent at $x/D=0.025$ and good at $x/D=0.23$.

Figure 4 presents the predicted and experimental swirl profiles along the y axis. It can be seen that the assumed radial distribution of the swirling body force is reasonable, but it slightly has too sharp a peak located too close to the propeller tip. Agreement between predictions and experiments is excellent and constitutes a major improvement over those of Ref. 4-6.

Figure 5 presents the predicted and experimental pressure profiles along the y axis. The pressure is given in the form of a pressure coefficient, $C_p=2(P-P_0)/(\rho U_0^2)$. These are the first viscous pressure predictions for this type of flow known to the authors. All analysis methods based on the boundary-layer equations require the specification of the pressure as input. The agreement with the experiments at $x/D=0.025$ is good. The pressure predicted at $x/D=0.23$ is in qualitative agreement with the theory of free-running propellers. The experimental profiles at $x/D=0.23$ have negative values typical of the flow over an obstacle such as the drive housing.

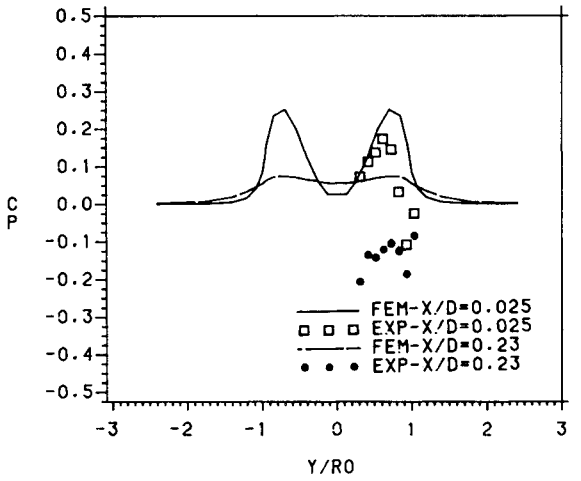

Fig. 5 Uniform flow: pressure profile.

Shear Flow Past a Propeller

This simulation of a free-running propeller in a shear flow corresponds to the experiments of Kotb.[16] The characteristics of the flow are:

$$U^*_{\text{inf}}=8.52-0.67y \text{ m/s}, \quad U_{\text{inf}}=1-0.1588y$$

$$\rho_0^*=1.177 \text{ kg/m}^3, \quad D^*=0.492 \text{ m}, \quad N=1150 \text{ rpm}$$

$$K_T=T^*/(\rho_0^* N^2 D^{*4})=0.158, \quad K_Q=Q^*/(\rho_0^* N^2 D^{*5})=0.0266$$

At the inflow and on the freestream shell boundary, U is set equal to the approach shear flow. All other boundary conditions are identical to those used for the uniform flow simulation.

To obtain an initial guess of the velocity field, a two-dimensional axisymmetric solution without swirl was produced for a uniform flow, and the velocity excess was extracted, rotated on the three-dimensional grid, and added to the approach shear flow. The system of nonlinear equations was then solved in two quasi-Newton iterations requiring a

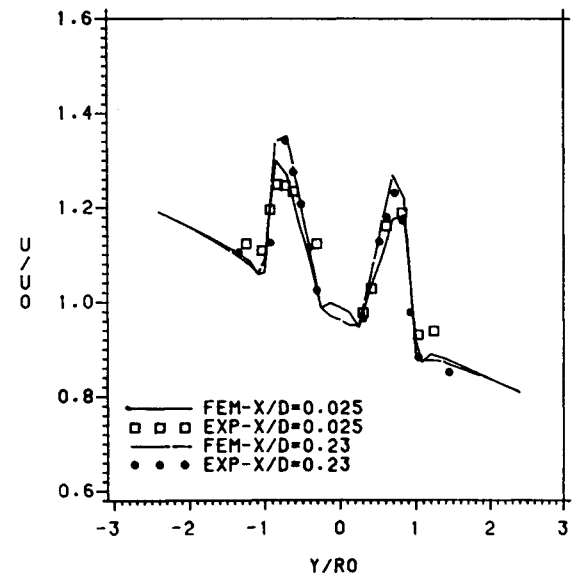

Fig. 6 Shear flow: axial velocity profile.

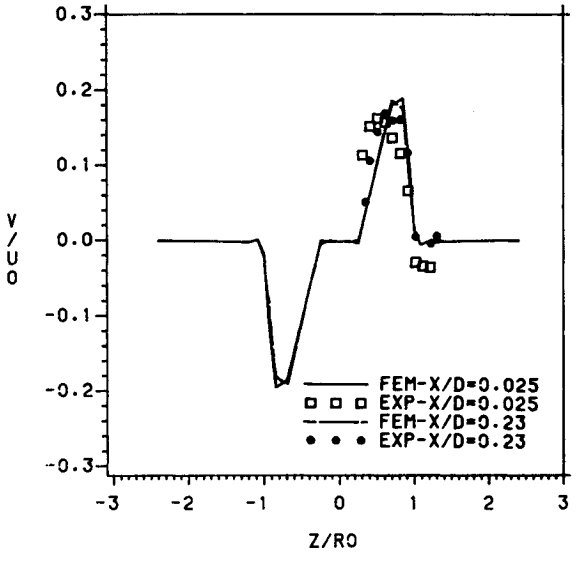

Fig. 7 Shear flow: swirl profile.

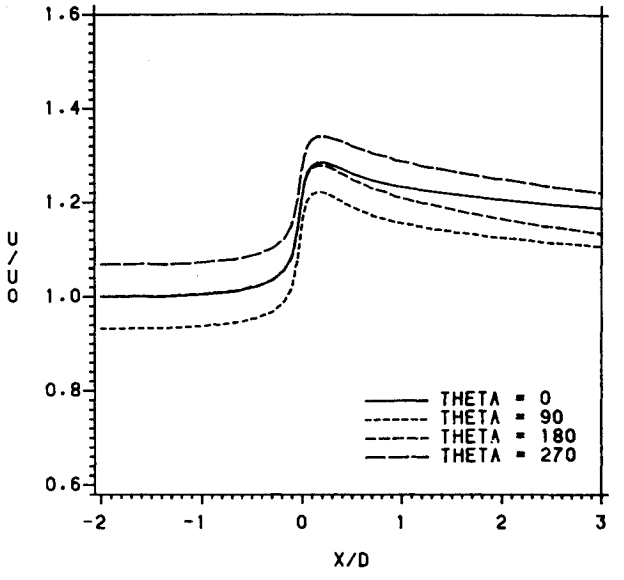

Fig. 9 Shear flow: streamwise velocity distribution.

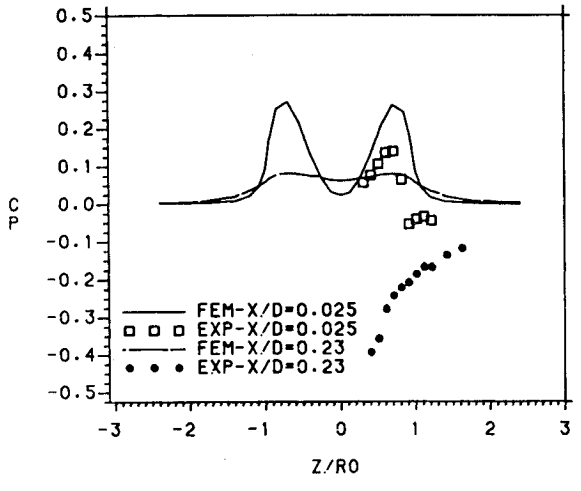

Fig. 8 Shear flow: pressure profile.

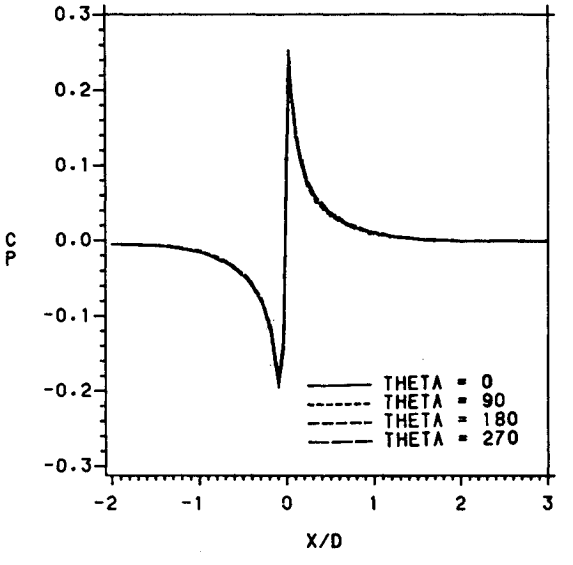

Fig. 10 Shear flow: streamwise pressure distribution.

total of 150 min of CPU on IBM-3081. No gradual introduction of thrust and torque in the course of the iteration was required as opposed to the work of Refs. 4-6.

Figure 6 compares the experimental and predicted axial velocity profiles along the y axis. The agreement is excellent at $x/D=0.025$ and good at $x/D=0.23$. On the low-speed side of the propeller, less fluid flows through the propeller and, hence, it is subject to more body force per unit mass flow. This results in higher acceleration of the fluid and a larger relative speed increase on the positive side of the y axis compared to the negative side. Figure 7 presents the predicted and experimental swirl profiles along the z axis. Agreement between predictions and experiments is excellent. Figure 8 gives the predicted and experimental pressure profiles along the y axis in the form of a pressure coefficient $C_p=2(P-P_0)/(\rho U_0^2)$. The experimental profiles have shapes similar to those of the predictions, but the amplitudes do not quite agree at $x/D=0.025$.

Figures 9-12 present predicted axial distributions of the axial component of the velocity, pressure, swirl, and radial velocity. These distributions were taken at a radius equal to 0.85 R, where the maximum thrust occurs. Figure 9 clearly shows the strong streamwise acceleration of the fluid upstream and downstream of the propeller. The variations in U at four peripheral locations are due to the shear flow. The two curves in the vertical plane display nonsymmetrical behavior. This is caused by the swirl that moves high-velocity fluid into regions of lower velocity, and vice versa. The significant upstream influence of the propeller on the pressure field is illustrated in Fig. 10. The sudden, almost discontinuous, pressure increase characteristic of actuator disks is evident. Figure 11 shows that there is negligible swirl upstream of the propeller, as predicted by vortex theory. The jump in the swirl across the propeller is a behavior akin to the shock wave in compressible flows. The small wiggles upstream of the propeller are typical of the use of Galerkin and central difference schemes for problems with sharp fronts. The near-perfect axial symmetry of the swirl distribution is observed. The slipstream contraction is clearly seen in Fig. 12.

Figure 13 presents axial velocity profiles along the y axis at various stations downstream of the propeller. The streamwise acceleration of the fluid downstream of the propeller due to pressure relaxation can be seen. The kinks near the tip of the propeller in the first two profiles of Fig. 13 are characteristic of flows past propellers.[16] The asymmetries due to the shear in the approach flow can be seen most clearly in the shape of the peaks of axial velocity. The swirl

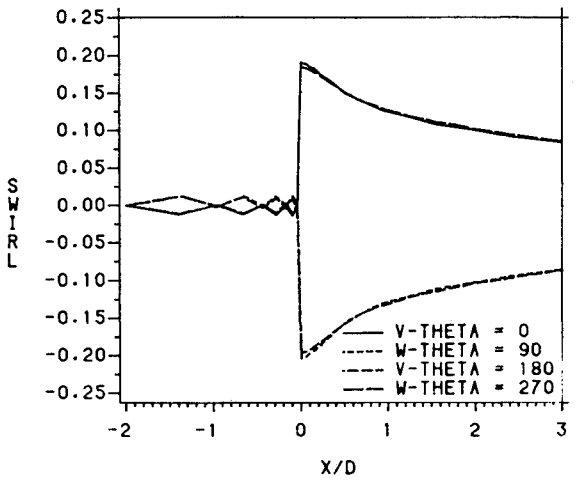

Fig. 11 Shear flow: streamwise swirl distribution.

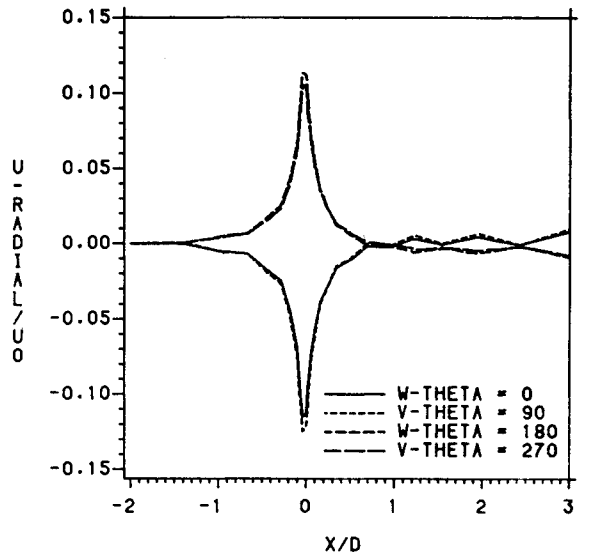

Fig. 12 Shear flow: streamwise radial velocity distribution.

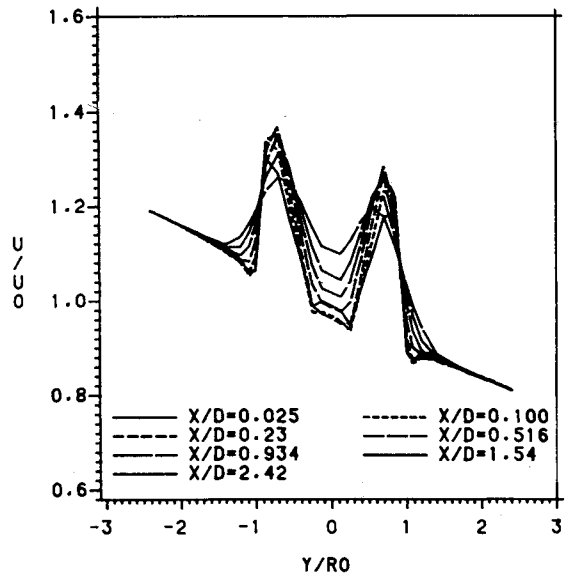

Fig. 13 Shear flow: axial velocity profiles.

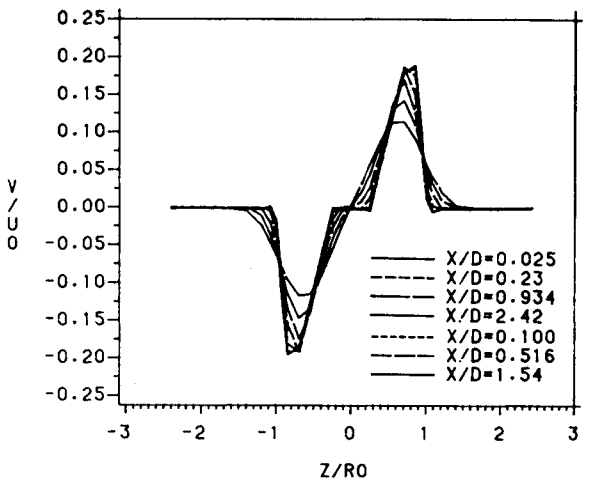

Fig. 14 Shear flow: swirl profiles.

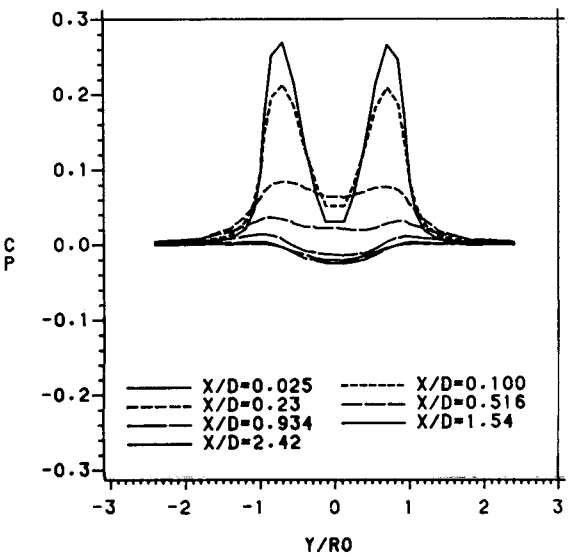

Fig. 15 Shear flow: pressure profiles.

profiles at various axial stations are shown in Fig. 14. The swirl level decays very slowly. The radial turbulent diffusion of momentum, characterized by flatter and wider profiles, is clearly seen. Pressure profiles are plotted in Fig. 15, illustrating the decay downstream of the propeller. The negative dimples in the last three curves are due to the zero axial traction applied to the outflow. The use of this natural boundary condition sets the pressure level at the outflow boundary. The axial traction is given by

$$t_x = -P + 2\mu_T U_{,x} = 0$$

where t_x is the axial traction and P the pressure. The zero traction defines the pressure level as

$$P = 2\mu_T U_{,x}$$

Since the axial velocity is still decaying, $U_{,x}$ is negative and the pressure at the exit takes a small negative value.

Conclusions

This work has developed a general-purpose, advanced computational technique for three-dimensional turbulent free shear flows past propellers. The main results can be sum-

marized as:

1) Predictions for uniform and shear flows past a propeller show excellent agreement with the experiments for the axial and swirl component of the velocity.

2) The simple turbulence model produced very accurate swirl predictions for both the uniform and shear flow cases. All previous numerical work on such flows provided poor predictions of swirl.

3) The pressure predictions presented here for viscous turbulent flows through a propeller are the first known to the authors.

4) The numerical simulations show that the propeller exerts a strong upstream influence on the axial and radial velocity fields, and on the pressure field. There is negligible swirl upstream of the propeller.

5) The resulting Galerkin finite element algorithm is robust and stable, mostly due to the full coupling of the three momentum equations and the continuity equation. It captured the complex features of the shear flow. No gradual introduction of the thrust and torque as the iteration proceeds is required as opposed to previous work.

Acknowledgment

This work is supported by the Office of Naval Research, with Dr. Choung Lee as Technical Monitor.

References

[1]Von Kármán, T. and Burgers, J. M., "General Aerodynamic Theory—Perfect Fluids," *Aerodynamic Theory*, Vol. 2, edited by W. F. Durand, California Institute of Technology, Pasadena, 1934.

[2]Sparenberg, J. A., "On the Potential Theory of the Interaction of an Actuator Disk and a Body," *Journal of Ship Research*, Vol. 16, Dec. 1972, pp. 271-277.

[3]Sparenberg, J. A., "On the Linear Theory of an Actuator Disk in a Viscous Flow," *Journal of Ship Research*, Vol. 18, No. 1, March 1974, pp. 16-21.

[4]Schetz, J. A. and Favin, S., Numerical Solution for the Near Wake of a Body with Propeller," *Journal of Hydronautics*, Vol. 11, Oct. 1977, pp. 136-144.

[5]Schetz, J. A. and Favin, S., "Numerical Solution of a Body-Propeller Combination Flow Including Swirl and Comparison with Data," *Journal of Hydronautics*, Vol. 13, April 1979, pp. 46-51.

[6]Schetz, J. A. and Figard, R. L., "Numerical Solution of the Flow Near the Rotor of a Wind Turbine," *Journal of Energy*, Vol. 6, March/April 1982, pp. 65-70.

[7]Pelletier, D. H., "Finite Element Solution of the Navier-Stokes Equations for 3-D Turbulent Free Shear Flows," Ph.D. Dissertation, Aerospace and Ocean Engineering Dept., Virginia Polytechnic Institute and State University, Blacksburg, Oct. 1984.

[8]Rodi W., *Turbulence Models and Their Application in Hydraulics*, International Association for Hydraulic Research, Delft, the Netherlands, 1980.

[9]Sforza, P. M., Steiger, M. H., and Trentacoste, N., "Studies on Three-Dimensional Viscous Jets," *AIAA Journal*, Vol. 4, May 1966, pp. 800-806.

[10]Hinze, J. O., *Turbulence*, 2d Ed., McGraw-Hill Book Co., New York, 1975.

[11]Reddy, J. N., "Penalty-Finite-Element Analysis of 3-D Navier-Stokes Equations," *Computer Methods in Applied Mechanics and Engineering*, Vol. 35, 1982, pp. 87-106.

[12]Reddy, J. N., "On Penalty Function Methods in the Finite Element Analysis of Flow Problems," *International Journal for Numerical Methods in Fluids*, Vol. 2, April-June 1982, pp. 151-172.

[13]Engelman, M. S., Strang, G., and Bathe, K.-J., "Application of Quasi-Newton Methods in Fluid Mechanics," *International Journal for Numerical Methods in Engineering*, Vol. 17, May 1981, pp. 707-718.

[14]Hasbani, Y. and Engelman, M. S., "Out of Core Solution of Linear Equations with a Non-Symmetric Coefficient Matrix," *Computers and Fluids*, Vol. 7, No. 1, March 1979, pp. 13-31.

[15]Engelman, M. S., "FIDAP: A Fluid Dynamics Analysis Program," *Advances in Engineering Software*, Vol. 4, No. 4, 1982, pp. 163-166.

[16]Kotb, M. A., "Experimental Investigation of 3-D Turbulent Free Shear Flows Past Propellers and Windmills," Ph.D. Dissertation, Aerospace and Ocean Engineering Department, Virginia Polytechnic Institute and State University, Blacksburg, VA, Oct. 1984.

[17]Schetz, J. A., *Foundations of Boundary Layer Theory for Momentum, Heat, and Mass Transfer*, Prentice-Hall, Englewood cliffs, NJ, 1984.

[18]Li, W.-H. and Lam, S.-H., *Principles of Fluid Mechanics*, Addison-Wesley Publishing Co., Reading, MA, 1964.